Article | Open Access

Energy Materials

Hu *et al. Energy Mater.* **2026**, *6*, 600129 **DOI:**10.20517/energymater.2026.173

Synergistic internal-external disorder to activate electrochemically inert maricite $NaFePO_4$

Wei Hu[1,#], Sen Dong[1,#], Yue Zhang[1,*], Bin Tang[2,*], Yifan Wu[3], Yakun Tang[1,*], Jinlin Li[4], Lang Liu[1], Zhen Zhou[2,4]

Keywords:
Defects, dynamic Jahn-Teller distortion, doping, lattice distortion, maricite $NaFePO_4$

Citation: Hu, W.; Dong, S.; Zhang, Y.; Tang, B.; Wu, Y.; Tang, Y.; Li, J.; Liu, L.; Zhou, Z. Synergistic internal-external disorder to activate electrochemically inert maricite $NaFePO_4$. *Energy Mater.* **2026**, *6*, 600129. https://dx.doi.org/10.20517/energymater.2026.173

Received: 13 Jun 2026
First Decision: 9 Jul 2026
Revised: 31 Aug 2026
Accepted: 15 Sep 2026
Published: 24 Sep 2026

Academic Editor:
Yuping Wu
Copy Editor:
Fangling Lan
Production Editor:
Fangling Lan

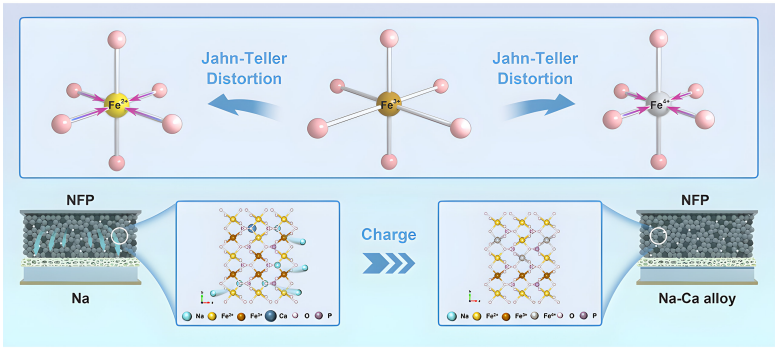

Abstract

$NaFePO_4$ (NFP) is a promising alternative to $LiFePO_4$, offering advantages such as the abundance of natural sodium resources. However, its common crystal phase, maricite, is typically electrochemically inert. This study presents a novel, synthesis-controllable, and rechargeable maricite NFP cathode material, specifically $Na_{0.33}Fe_{0.95}Ca_{0.06}PO_4$, for sodium-ion batteries. The structure provides two main benefits: Ca^{2+} doping broadens the bulk sodium-ion transport channels, while the dynamic and persistent Jahn-Teller distortion caused by the coexistence of Fe^{4+}, Fe^{3+}, and Fe^{2+} induces internal lattice distortion, effectively activating its electrochemical activity. Additionally, nanocrystallization introduces external structural disorder, further shortening the ion diffusion path. This cathode exhibits a high reversible capacity of 178.6 mAh g^{-1} at 50 mA g^{-1} and a material-based energy density of 415 Wh kg^{-1}. This study offers a general strategy for activating

[1]Key Laboratory of Energy Materials Chemistry, Ministry of Education, College of Chemistry, Xinjiang University, Urumqi 830017, Xinjiang, China.
[2]Interdisciplinary Research Center for Sustainable Energy Science and Engineering (IRC4SE2), School of Chemical Engineering, Zhengzhou University, Zhengzhou 450001, Henan, China.
[3]Future Battery Research Center, Global Institute of Future Technology, Shanghai Jiao Tong University, Shanghai 200240, China.
[4]Institute of New Energy Material Chemistry, Renewable Energy Conversion and Storage Center (ReCast), School of Materials Science and Engineering, Nankai University, Tianjin 300350, China.
[#]Authors contributed equally.

[*]**Correspondence to:** Prof. Yue Zhang, Prof. Yakun Tang, Key Laboratory of Energy Materials Chemistry, Ministry of Education, College of Chemistry, Xinjiang University, Urumqi 830017, Xinjiang, China. E-mail: yuezhang@xju.edu.cn; yktang@xju.edu.cn; Dr. Bin Tang, Interdisciplinary Research Center for Sustainable Energy Science and Engineering (IRC4SE2), School of Chemical Engineering, Zhengzhou University, Zhengzhou 450001, Henan, China. E-mail: tangbin@zzu.edu.cn

electrochemically inert yet potentially viable battery materials, providing new insights for developing next-generation, high-performance, and low-cost energy storage systems.

INTRODUCTION

Sodium-ion batteries have demonstrated significant potential for large-scale energy storage due to the abundance of sodium resources, low cost, and environmental friendliness[1-5]. Among various cathode materials, $NaFePO_4$ (NFP) is considered a highly promising candidate because of its chemical similarity to the industrialized and commercialized lithium-based cathode material, $LiFePO_4$[6-9]. Although olivine NFP offers a high theoretical specific capacity of 155 mAh g^{-1}, its practical application is hindered by thermodynamic instability and complex synthesis routes[10-12]. In contrast, the thermodynamically favored maricite NFP has been shown to be electrochemically inactive due to its closed framework structure, which lacks effective Na^+ diffusion pathways within the crystal lattice[13-16]. Furthermore, the inherently low electronic conductivity of phosphate-based electrode materials further limits their practical use[17]. Therefore, developing rational and efficient modification strategies to construct sodium-ion diffusion channels and enhance the conductivity of maricite NFP has become a key research focus.

To overcome the intrinsic ion transport limitations of NFP, various modification strategies have been proposed. One common approach is reducing particle size to shorten the sodium-ion diffusion pathway[18,19]. Liu *et al.*[20] prepared ultra-fine maricite $NaFePO_4$@C nanoparticles (3 nm) assembled into NFP nanoclusters, which deliver a high reversible capacity of 149.2 mAh g^{-1} at 0.2 C and exhibit excellent rate capability. Carbon coating has also been employed to construct conductive networks and improve electron transport[21]. Wang *et al.*[22] synthesized NFP composites with an ultrathin carbon coating of 2-3 nm, demonstrating a reversible capacity of 135 mAh g^{-1} at 0.1 C. Structural design represents another effective route for enhancing conductivity. Ma *et al.*[16] embedded maricite NFP nanoparticles into micro-grooved carbon cloth, resulting in a high capacity of 142 mAh g^{-1} at 0.1 C. Although these methods have proven effective, they primarily rely on physical modifications of the surface or interface, without fundamentally addressing the lack of intrinsic sodium-ion transport channels within the NFP crystal structure. Therefore, an innovative strategy that intrinsically reconstructs sodium-ion migration pathways at the crystal-structure level is urgently needed.

To address these challenges, this study proposes a novel cathode material for sodium-ion batteries: $Na_{0.33}Fe_{0.95}Ca_{0.06}PO_4$ (denoted as NFP/C-$HT_{0.02}$). The crystal disorder induced by the dynamic Jahn-Teller effect, combined synergistically with Ca^{2+} doping, broadens sodium-ion migration pathways and reduces the diffusion energy barrier, thereby significantly enhancing bulk ionic conductivity. Additionally, the implementation of a nanostructuring strategy introduces external structural disorder. This unique "internal-external synergistic disordering" structural design reconstructs the sodium-ion transport pathways at the crystalline level, markedly improving sodium-ion transport kinetics and the electrochemical activity of the material. Benefiting from this distinctive structure, the cathodes exhibit outstanding electrochemical performance, achieving a high reversible capacity of 178.6 mAh g^{-1} at a current density of 50 mA g^{-1} and an energy density of 415 Wh kg^{-1}.

EXPERIMENTAL

Material synthesis

Graphite oxide was dispersed in deionized water, followed by the addition of equimolar amounts of $Fe(NO_3)_3 \cdot 9H_2O$, NaH_2PO_4, and citric acid. The mixture was continuously stirred at 80 °C until a homogeneous sol formed, which was then dried to obtain the precursor. This precursor was freeze-dried, ground, and subsequently calcined at 350 °C for 4 h, followed by calcination at 600 °C for 8 h under an Ar/H_2 atmosphere. The resulting product was designated NFP/C.

The NFP/C material was stirred in a 0.3 M HCl solution for 1 h and then washed until neutral, yielding the acid-treated product labeled NFP/C H. In a separate procedure, the precursor was mixed with nano $CaCO_3$ at a mass ratio of 1:0.01, ground, and uniformly dispersed in deionized water. After freeze-drying and calcination under the same conditions described above, the resulting product was washed and designated NFP/C $T_{0.01}$.

Furthermore, the precursor was mixed with nano-$CaCO_3$ at mass ratios of 1:0.01, 1:0.02, and 1:0.03, respectively. Each mixture was homogenized in deionized water, freeze-dried, ground, and calcined under identical conditions. The calcined products were then ground again, stirred in diluted HCl for 1 h, and washed until neutral. The final products were labeled NFP/C-$HT_{0.01}$, NFP/C-$HT_{0.02}$, and NFP/C-$HT_{0.03}$, respectively.

Material characterization

The elemental composition of the samples was determined by inductively inductively coupled plasma optical emission spectrometry (ICP-OES) using an Optima 8000 instrument. The crystal structure was analyzed with an X-ray diffractometer (XRD, SmartLab SE) employing Cu Kα radiation. The carbon content of the materials was measured by thermogravimetric analysis (TGA) using a HITACHI STA7300. The chemical states of surface elements were investigated *via* X-ray photoelectron spectroscopy (XPS) with a Thermo Scientific K-Alpha system. X-ray absorption fine structure (XAFS) spectroscopy was performed in transmission mode on a Rapid XAFS 2M instrument (Anhui Absorption Spectroscopy Instrument Co., Ltd.) at 20 kV and 20 mA. For iron analysis, a Ge (620) spherical bent crystal analyzer with a curvature radius of 500 mm was employed. The morphology and structural characteristics of the materials were examined by scanning electron microscopy (SEM, Hitachi S-4800), transmission electron microscopy (TEM, FEI Tecnai F20), high-resolution TEM (HRTEM), selected-area electron diffraction (SAED), and energy-dispersive X-ray spectroscopy (EDS) elemental mapping. Dispersion stability was evaluated using a zeta potential analyzer (Zetasizer Pro 46500). Nitrogen adsorption-desorption isotherms were obtained with an Autosorb-iQ physisorption analyzer (Micromeritics APSP 2460). The specific surface area was calculated using the Brunauer-Emmett-Teller (BET) method, and the pore size distribution was determined by the Barrett-Joyner-Halenda model.

Electrochemical measurements

The electrochemical performance of the samples was evaluated using a LAND battery test system (CT2001A, Wuhan, China) and a CHI760D electrochemical workstation. The active material, Ketjen black, and polyvinylidene fluoride were mixed in a mass ratio of 7:2:1 and dispersed in N-methyl-2-pyrrolidone (NMP) to form a homogeneous slurry. This slurry was cast onto carbon-coated aluminum foil and dried to form the cathode. The electrode films were vacuum-dried at 110 °C for 12 h. The mass of active material on each electrode sheet was approximately 0.8 mg. Coin-type half-cells were assembled in an argon-filled glove box. The cathode electrolyte (TC-E201) was purchased from Tianjin Tianchi Materials Technology Co., Ltd. Metallic sodium was used as both the counter and reference electrode. Electrochemical measurements of the cathodes were conducted within a voltage range of 1.5 to 4.3 V. Electrochemical impedance spectroscopy (EIS) was recorded over a frequency range of 0.01 Hz to 100 kHz. The electrolyte consisted of 1 M $NaClO_4$ in a mixture of ethylene carbonate and propylene carbonate (v/v, 1:1), with 5% fluoroethylene carbonate added as a high-voltage additive. A glass fiber GF/F membrane was used as the separator.

RESULTS

Electrochemical activation of maricite NFP

The samples were prepared using a conventional sol-gel method. A schematic illustration of the synthesis process is presented in Figure 1A. To elucidate the individual and combined effects of the nano-$CaCO_3$ template and HCl washing, control samples NFP/C-$T_{0.01}$ and NFP/C-H were also synthesized. The XRD

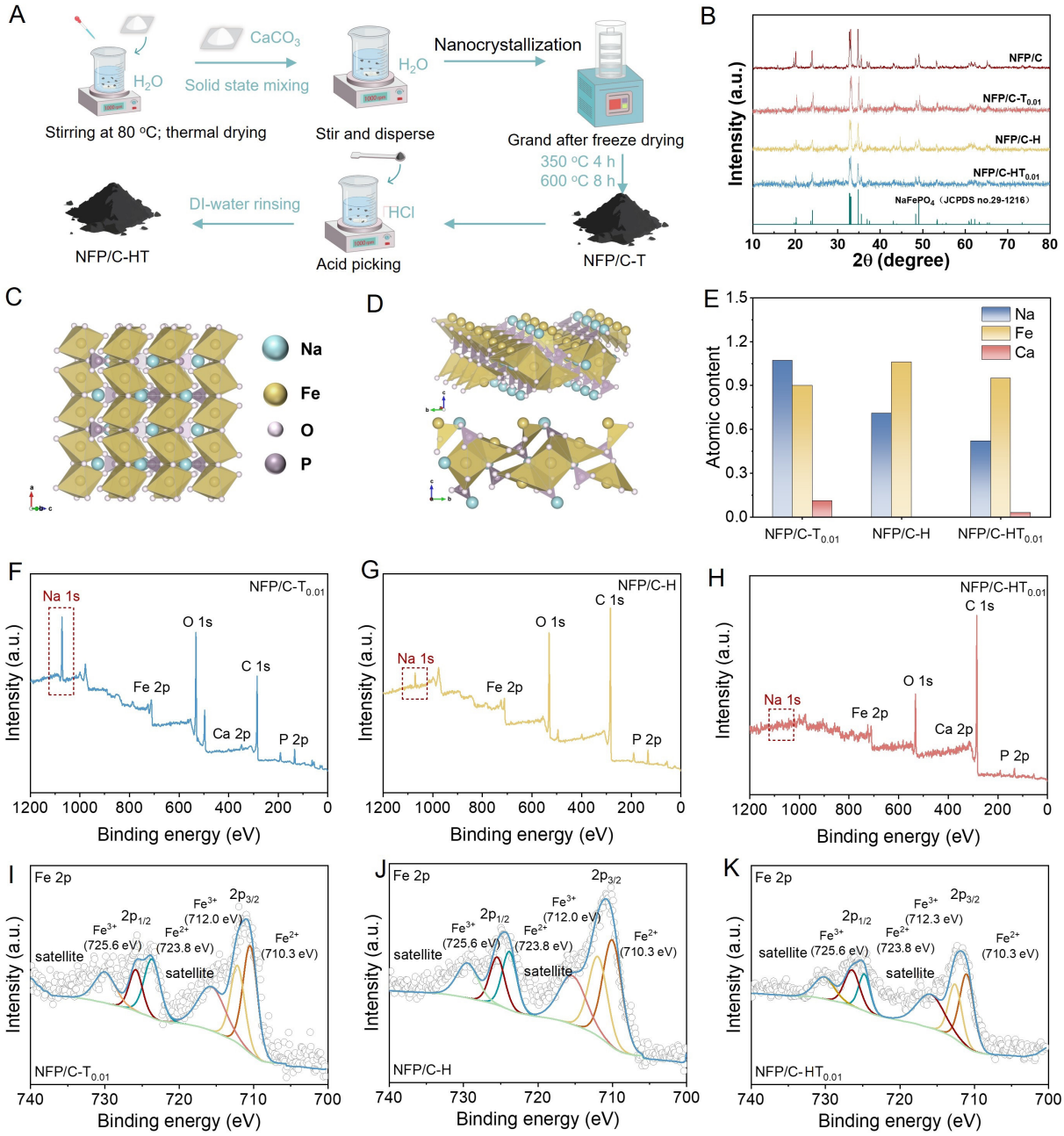

Figure 1. Sample preparation and structural characterizations. (A) Schematic diagram of the synthesis process for the NFP/C-HT sample; (B) XRD patterns of NFP/C, NFP/C-$T_{0.01}$, NFP/C-H, and NFP/C-$HT_{0.01}$ samples; (C) schematic of the maricite NFP crystal; (D) crystal structure diagram sectioned along the (111) plane; (E) ICP results for the NFP/C-$T_{0.01}$, NFP/C-H, and NFP/C-$HT_{0.01}$ samples; (F-H) full XPS spectra of samples NFP/C-$T_{0.01}$, NFP/C-H, and NFP/C-$HT_{0.01}$; and (I-K) Fe 2p XPS spectra of NFP/C-$T_{0.01}$, NFP/C-H, and NFP/C-$HT_{0.01}$.

patterns of NFP/C, NFP/C-$T_{0.01}$, NFP/C-H, and NFP/C-$HT_{0.01}$ are shown in Figure 1B. All diffraction peaks correspond well with the reference pattern of maricite NFP (JCPDS no. 29-1216)[23], and no impurity peaks were detected, confirming the phase purity of the as-prepared samples. Notably, NFP/C exhibits the sharpest diffraction peaks, indicating the highest crystallinity[24]. In contrast, NFP/C-$T_{0.01}$, which includes the template agent, shows weakened peak intensities. The acid-washed sample NFP/C-H displays a significant reduction in peak intensity, while the NFP/C-$HT_{0.01}$ sample, treated with both templating and acid washing, demonstrates the lowest crystallinity[25], indicating that the combined treatment effectively reduces the material's crystallinity and likely introduces a considerable number of random crystal defects, thereby disrupting its long-range ordered structure.

The morphology of the samples was characterized by SEM [Supplementary Figure 1]. As shown in [Supplementary Figure 1A, the NFP/C sample exhibits large, block-like structures with significant aggregation. After introducing the templating agent, the NFP/C-$T_{0.01}$ sample [Supplementary Figure 1B] displays a markedly reduced particle size, forming uniform spherical particles with less agglomeration. Further acid washing of the NFP/C-H sample [Supplementary Figure 1C] results in even finer particles and increased surface roughness, indicating that the acid treatment effectively disrupts the surface structure and promotes particle refinement of maricite NFP. The reduction in particle size increases the specific surface area, providing more active sites for sodium-ion insertion and extraction, thereby enhancing electrode reaction kinetics[26,27]. Additionally, both templating and acid washing contribute to a more developed porous structure, further optimizing the material architecture[28-30]. Zeta potential measurements [Supplementary Figure 2] indicate a higher surface charge density for both NFP/C-$T_{0.01}$ and NFP/C-H. This enhanced electrostatic repulsion, combined with their reduced particle size, effectively suppresses agglomeration and promotes dispersion stability[31,32].

The morphology of NFP/C-$T_{0.01}$ and NFP/C-H was further examined using TEM. As shown in Supplementary Figure 1D and E, the NFP/C-$T_{0.01}$ sample consists of relatively large particles uniformly coated with graphene sheets. The HRTEM image [Supplementary Figure 1F] reveals clear lattice fringes with spacings of 0.36 and 0.26 nm, corresponding to the (111) and (301) planes of maricite NFP, respectively[18]. The SAED pattern (inset of Supplementary Figure 1F) exhibits distinct diffraction rings indexed to the (111) and (301) planes, further confirming the maricite-type structure[21]. In contrast, the NFP/C-H [Supplementary Figure 1G and H] displays smaller particle sizes and improved dispersion, consistent with the SEM observations. The HRTEM image [Supplementary Figure 1I] shows lattice fringes of 0.26 nm, assigned to the (301) plane of maricite NFP, indicating that the material retains a certain degree of crystallinity at the microscopic scale. The presence of only a few discrete diffraction spots in the SAED pattern (inset of Supplementary Figure 1I) suggests lower crystallinity compared with NFP/C-$T_{0.01}$, which can be attributed to the loss of sodium ions during acid washing, resulting in the formation of sodium-deficient defects. EDS elemental mapping of NFP/C-$T_{0.01}$ [Supplementary Figure 1J] confirms a homogeneous distribution of Na and Fe throughout the material. Additionally, a thin carbon coating is observed on the material's surface.

Figure 1C illustrates the crystal structure of maricite NFP, with additional orientations shown in Supplementary Figure 3. TEM analysis confirms that the (111) plane is the primary exposed facet, and a cross-sectional view of this plane is presented in Figure 1D. In the pristine maricite structure, sodium ions are confined between [FeO_6] octahedra and [PO_4] tetrahedra within a closed framework, which impedes efficient Na^+ diffusion and results in electrochemical inactivity. In contrast, after our processing method, the (111) facet in maricite NFP effectively exposes sodium ions, facilitating their release from the lattice and enabling rapid Na^+ transport.

ICP-OES analysis was performed to examine the chemical composition [Figure 1E]. A trace amount of Ca was detected in NFP/C-$T_{0.01}$, accompanied by partial Fe loss, suggesting possible lattice doping by the templating agent. It should be noted that the samples were thoroughly washed, eliminating the possibility of Ca residue. In the acid-treated sample NFP/C-H, the Na content decreased to 0.71, indicating the formation of sodium vacancies while the maricite structure remained intact, as confirmed by XRD [Figure 1B]. These results demonstrate that the template mildly tunes the composition and microstructure of maricite NFP, whereas acid washing introduces sodium defects and disrupts the long-range order. This structural change breaks the closed framework and creates efficient pathways for Na^+ migration. The surface chemical states of NFP/C-$T_{0.01}$, NFP/C-H, and NFP/C-$HT_{0.01}$ were analyzed by XPS. As shown in Figure 1F-H, all samples contain Na, Fe, P, O, and C as the primary elements. The acid-washed samples NFP/C-H and NFP/C-$HT_{0.01}$

exhibit a clear reduction in Na XPS intensity, further confirming sodium loss due to acid treatment. Trace Ca is detected in the templated samples NFP/C-$T_{0.01}$ and NFP/C-$HT_{0.01}$, consistent with ICP-OES results. The Fe 2p XPS spectra are presented in Figure 1I-K. A higher binding energy is observed for the Fe 2p peaks in NFP/C-H and NFP/C-$HT_{0.01}$, indicating an elevated Fe oxidation state[33,34]. This shift results from charge compensation following Na^+ removal, which promotes the oxidation of Fe^{2+} to Fe^{3+}. Peak fitting analysis [Supplementary Figure 4] further reveals a progressive increase in the Fe^{3+}/Fe^{2+} ratio with sodium deficiency, confirming that acid treatment induces redox reactions and modifies the Fe valence distribution.

Raman spectroscopy was performed on NFP/C-$T_{0.01}$, NFP/C-H, and NFP/C-$HT_{0.01}$ to investigate the defect structure of the amorphous carbon in the composites. As shown in Supplementary Figure 5, all samples exhibit distinct characteristic peaks at 1,586.5 cm^{-1} (G band, representing graphitic carbon) and 1,343.2 cm^{-1} (D band, associated with structural defects)[35,36]. The I_D/I_G ratios for NFP/C-$T_{0.01}$, NFP/C-H, and NFP/C-$HT_{0.01}$ are 0.78, 0.91, and 0.92, respectively. The higher I_D/I_G values of NFP/C-H and NFP/C-$HT_{0.01}$ indicate a lower degree of structural order in the carbon, suggesting that acid treatment effectively disrupts the surface regularity and introduces more defects and disordered structures[37]. Among them, NFP/C-$HT_{0.01}$ shows the highest I_D/I_G ratio, reflecting the greatest defect concentration and structural disorder in its carbon layers. These structural defects can serve as active sites during electrochemical processes, thereby enhancing reaction activity. The specific surface area and pore structure of the samples were characterized by BET measurements. As shown in Supplementary Figure 6A, all samples display type IV isotherms with clear hysteresis loops in the P/P_0 range of 0.4-1.0, confirming their mesoporous nature. The specific surface areas of NFP/C-$T_{0.01}$, NFP/C-H, and NFP/C-$HT_{0.01}$ are 52.0, 109.7, and 123.7 $m^2 \cdot g^{-1}$, respectively. The markedly higher surface area of the acid-treated samples suggests that acid treatment induces surface restructuring and increases the accessible area, consistent with SEM and zeta potential analyses. Pore size distribution profiles [Supplementary Figure 6B] show that NFP/C-$HT_{0.01}$ exhibits the most developed porosity with abundant mesopores. Its hierarchical pore structure enhances electrolyte infiltration and ionic diffusion, supporting fast ion transport and improved electrode reaction kinetics.

The electrochemical performance of the prepared cathodes was evaluated in coin-type half-cells over a voltage range of 1.5 to 4.3 V. At a current density of 100 mA g^{-1} [Supplementary Figure 7A], the initial discharge capacities of NFP/C, NFP/C-$T_{0.01}$, NFP/C-H, and NFP/C-$HT_{0.01}$ were 55.8, 67.2, 79.8, and 96.0 mAh g^{-1}, respectively. Among these, NFP/C-$HT_{0.01}$ exhibited the highest reversible capacity and retained 93.3% of its initial capacity after 100 cycles, demonstrating excellent cycling stability. This enhancement is attributed to the tailored microstructure and increased lattice disorder. Smaller particles mitigate volume strain during Na^+ insertion and extraction, thereby improving structural integrity. Additionally, the larger specific surface area provides more Na^+ storage sites and accelerates electrode kinetics. Furthermore, the disordered framework induced by sodium vacancies, combined with Ca^{2+} incorporation, creates additional ion transport pathways, thereby activating the electrochemical activity of maricite NFP.

Rate performance data are presented in Supplementary Figure 7B. NFP/C-$HT_{0.01}$ delivers capacities of 112.1, 94.8, 84.9, 79.5, 75.9, and 69.4 mAh g^{-1} at current densities of 0.05, 0.1, 0.2, 0.3, 0.5, and 1 A g^{-1}, respectively. When the current density is returned to 0.05 A g^{-1}, the capacity recovers to 110.4 mAh g^{-1}, demonstrating excellent reversibility and rate capability. These results confirm that the combination of templating and acid treatment effectively optimizes the microstructure and lattice disorder of NFP/C-$HT_{0.01}$. The resulting porous network and sodium defects synergistically facilitate Na^+ diffusion, underpinning the remarkable cycling stability and rate performance.

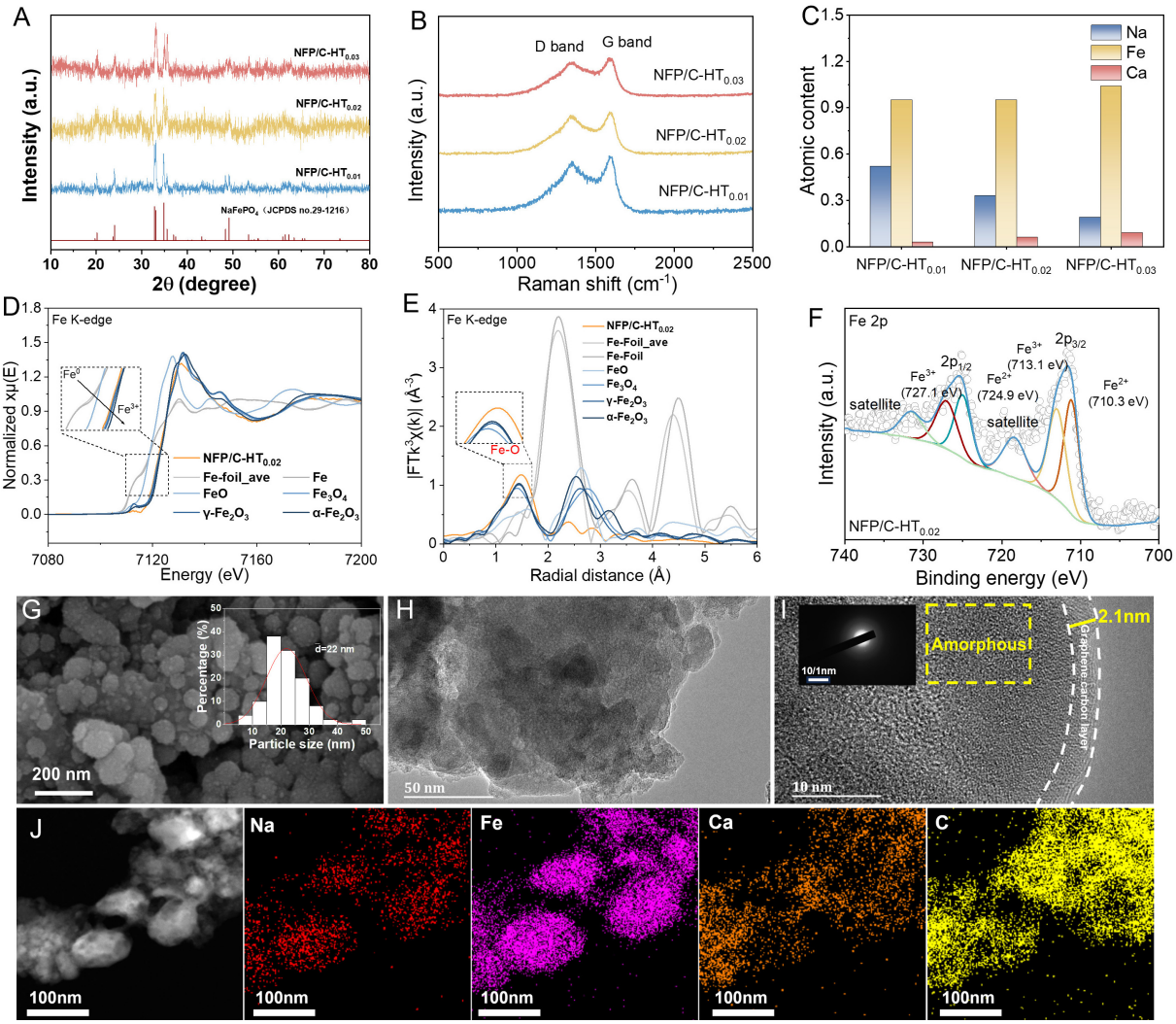

Figure 2. Structural characterizations: (A) XRD patterns of NFP/C-HT$_{0.01}$, NFP/C-HT$_{0.02}$, and NFP/C-HT$_{0.03}$ samples; (B) Raman spectra of NFP/C-HT$_{0.01}$, NFP/C-HT$_{0.02}$, and NFP/C-HT$_{0.03}$ samples; (C) ICP results for NFP/C-HT$_{0.01}$, NFP/C-HT$_{0.02}$, and NFP/C-HT$_{0.03}$ samples; (D) XANES spectra of NFP/C-HT$_{0.02}$; (E) normalized Fe EXAFS spectra of NFP/C-HT$_{0.02}$; (F) Fe 2p spectra of NFP/C-HT$_{0.02}$; (G-J) SEM, TEM, HRTEM, and EDS images of NFP/C-HT$_{0.02}$ (inset shows the particle size distribution histogram).

Excavating the electrochemical potential of maricite NFP

To investigate the influence of the template ratio on electrochemical behavior, NFP/C HT$_{0.02}$ and NFP/C HT$_{0.03}$ were synthesized with precursor-to-template mass ratios of 1:0.02 and 1:0.03, respectively. XRD patterns [Figure 2A] show that both samples retain the maricite-type NFP crystal structure. As the template ratio increases, the intensity of the diffraction peaks gradually decreases, indicating reduced crystallinity and increased structural disorder. Rietveld full-pattern refinements yield lattice parameters for pristine NFP (a = 8.986 Å, b = 6.869 Å, c = 5.045 Å) [Supplementary Figure 8A] and NFP/C HT$_{0.02}$ (a = 8.895 Å, b = 6.870 Å, c = 5.046 Å) [Supplementary Figure 8B]. Upon Ca^{2+} substitution, a slight contraction of the a-axis occurs, while the b- and c-axes remain nearly unchanged. This anisotropic lattice change induces lattice strain and local structural rearrangement, which modulates the geometric configuration of Na^+-migration tunnels. Such lattice-distorted local environments are beneficial for Na-ion transport and enhance electrochemical performance.

Raman spectroscopy was employed to investigate the effect of the template ratio on the carbon structural order of NFP/C-HT$_{0.02}$ and NFP/C-HT$_{0.03}$ [Figure 2B]. Both samples exhibit characteristic G band (1,586.5 cm^{-1}) and D band (1,343.2 cm^{-1}) peaks. The I_D/I_G ratio of NFP/C-HT$_{0.02}$ is 0.94, higher than that of

$NFP/C\text{-}HT_{0.03}$ (0.88), indicating greater structural disorder and defect density in its carbon matrix. TGA analysis [Supplementary Figure 9] reveals a carbon content of 7.1 wt% for $NFP/C\text{-}HT_{0.02}$. Notably, the slight weight gain observed between 280 and 350 °C is attributed to the oxidation of surface Fe^{2+} species to Fe^{3+} in air.

To investigate the surface and porous structural characteristics, N_2 adsorption-desorption tests were performed [Supplementary Figure 10A]. $NFP/C\text{-}HT_{0.02}$ exhibits a specific surface area of 192.1 $m^2 g^{-1}$ and a pore volume of 0.42 $cm^3 g^{-1}$, both significantly higher than those of $NFP/C\text{-}HT_{0.03}$ (162.8 $m^2 g^{-1}$ and 0.35 $cm^3 g^{-1}$, respectively). The larger specific surface area provides abundant electroactive sites, while the increased pore volume accommodates sufficient electrolyte and continuous transport channels, reducing sodium ion diffusion resistance and collectively facilitating rapid ion transport. The pore size distribution [Supplementary Figure 10B] further confirms that $NFP/C\text{-}HT_{0.02}$ possesses well-developed hierarchical pores. Macropores enable rapid electrolyte infiltration and accommodate lattice volume changes during cycling, whereas mesopores shorten the solid-state diffusion pathway of Na^+ ions and expose numerous redox-active sites. The synergistic effect of this dual pore architecture significantly accelerates ion transport and optimizes the interfacial reaction kinetics of the electrode. ICP-OES data reveal a continuous decline in sodium content as the template ratio increases [Figure 2C]. The molar ratios of Na:Fe:Ca in $NFP/C\text{-}HT_{0.01}$, $NFP/C\text{-}HT_{0.02}$, and $NFP/C\text{-}HT_{0.03}$ are 0.52:0.95:0.03, 0.33:0.95:0.06, and 0.19:1.04:0.09, respectively. Although $NFP/C\text{-}HT_{0.03}$ exhibits the lowest sodium content, excessive sodium loss may lead to the collapse of the NFP crystal structure.

The Fe K-edge X-ray absorption near-edge structure (XANES) spectra [Figure 2D] exhibit a distinct shift to higher energy for $NFP/C\text{-}HT_{0.02}$ compared to low-valent references (FeO, Fe foil), indicating an iron oxidation state approaching +3. This shift is attributed to the loss of sodium ions, which triggers the oxidation of some Fe^{2+} to Fe^{3+} to maintain charge balance, resulting in a mixed Fe^{2+}/Fe^{3+} valence state. The presence of mixed Fe^{2+}/Fe^{3+} valence is crucial for inducing structural disorder. In pristine NFP, the absence of Fe^{3+} ensures high structural stability without Jahn-Teller distortion. However, the introduction of low-spin $Fe^{3+}(t_{2g}^5 e_g^0)$ promotes Jahn-Teller distortion around high-spin $Fe^{2+}(t_{2g}^4 e_g^2)$ centers, leading to local lattice distortion and further structural disorder. This disordered configuration broadens sodium migration pathways and enhances Na^+ diffusion kinetics[38,39].

The Fourier transform-extended X-ray absorption fine structure (FT-EXAFS) spectrum of $NFP/C\text{-}HT_{0.02}$ [Figure 2E] reveals a significant increase in the Fe-O bond length. This change can be attributed to local lattice distortion induced by the Jahn-Teller effect, which optimizes the electronic structure and enhances electron transport within the electrode material, thereby facilitating faster electron transfer during charge and discharge processes[40]. In the Fe 2p XPS spectra [Figure 2F], the Fe 2p peaks shift further toward higher binding energies, indicating a gradual increase in the iron oxidation state. This shift results from the oxidation of Fe^{2+} to Fe^{3+} to maintain charge balance during desodiation, leading to an elevated average Fe oxidation state. This conclusion is consistent with the absorption edge shift observed in the XANES spectra.

The SEM characterization [Figure 2G] reveals that $NFP/C\text{-}HT_{0.02}$ consists of small nanospheres with an average particle size of approximately 22 nm and significantly improved dispersion. This refined microstructure increases the specific surface area, facilitating rapid Na^+ insertion and extraction while reducing volume strain during cycling, thereby enhancing structural stability and cycle life[41]. In contrast, although $NFP/C\text{-}HT_{0.03}$ also exhibits a nano-spherical morphology [Supplementary Figure 11A and B], the excess template causes pore collapse and severe particle agglomeration, resulting in poor dispersion. This observation is further supported by zeta potential measurements shown in Supplementary Figure 12.

TEM images [Figure 2H] reveal a uniform graphene coating on the nanospheres in NFP/C-HT$_{0.02}$, which enhances electrical conductivity and provides additional pathways for Na^+ migration. HRTEM [Figure 2I] shows no distinct lattice fringes, and the corresponding SAED pattern lacks clear diffraction rings, confirming a highly disordered structure. This disorder, induced by Jahn-Teller lattice distortion, facilitates Na^+ migration by lowering the diffusion energy barrier and creating more ion transport channels. Furthermore, the NFP/C-HT$_{0.02}$ particles are uniformly coated with an amorphous carbon layer approximately 2.1 nm thick. This thin, continuous carbon shell accelerates electron conduction, shortens Na^+ diffusion distances, and buffers lattice volume changes during sodiation and desodiation, synergistically enhancing the electrode's electrochemical kinetics and cycling stability. EDS mapping [Figure 2J] demonstrates a homogeneous distribution of Na, Fe, and C, with Na content notably lower than Fe, consistent with ICP-OES results. Trace Ca, derived from the template agent, is also detected.

The electrochemical performance of the as-prepared cathodes was evaluated using coin-type half-cells within a voltage range of 1.5-4.3 V. As shown in the cyclic voltammetry (CV) curves [Figure 3A], NFP/C-HT$_{0.01}$, NFP/C-HT$_{0.02}$, and NFP/C-HT$_{0.03}$ all exhibit a pair of redox peaks at approximately 2.1 and 2.9 V, corresponding to the Fe^{2+}/Fe^{3+} redox reaction associated with Na^+ extraction and insertion. Notably, NFP/C-HT$_{0.02}$ displays sharper and more symmetric redox peaks, indicating enhanced electrochemical reversibility and improved charge transfer kinetics. This improved performance is attributed to the highly disordered structure induced by the Jahn-Teller effect, combined with Ca^{2+} incorporation, which synergistically promotes rapid Na^+ diffusion. EIS measurements [Figure 3B] further reveal that NFP/C-HT$_{0.02}$ possesses the smallest charge transfer resistance (*Rct*), significantly lower than those of NFP/C-HT$_{0.01}$ and NFP/C-HT$_{0.03}$, confirming its superior ion electrochemical kinetic characteristics. At a current density of 100 mA g^{-1}, NFP/C-HT$_{0.02}$ delivers an initial charge capacity of 65.1 mAh g^{-1} [Figure 3C]. The theoretical specific capacity of NFP/C-HT$_{0.02}$ is 55.9 mAh g^{-1}, calculated from the ICP-OES-derived formula of $Na_{0.33}Fe_{0.95}Ca_{0.06}PO_4$ (molar mass 158.02 g mol^{-1}). The slightly higher initial charge capacity relative to the theoretical value is mainly attributed to the additional extraction of Ca^{2+} and partial oxidation of Fe^{3+} to Fe^{4+} during the first charge.

The slightly higher charging capacity may be attributed to the extraction of Ca^{2+} from the crystal structure. During the discharging process, a high reversible capacity of 148.7 mAh g^{-1} is achieved. Even after 100 cycles, a reversible capacity of 128.3 mAh g^{-1} is maintained [Figure 3D]. The rate performance evaluated at different current densities is shown in Figure 3E. NFP/C-HT$_{0.02}$ exhibits outstanding rate capability, delivering reversible capacities of 178.6, 149.4, 128.6, 112.6, 108.7, and 93.8 mAh g^{-1} at current densities ranging from 0.05 to 1 A g^{-1}. This high reversible capacity of 178.6 mAh g^{-1} corresponds to the reversible insertion and extraction of one electron per formula unit of the $Na_{0.33}Fe_{0.95}Ca_{0.06}PO_4$ cathode. In contrast, NFP/C-HT$_{0.03}$ shows poor rate performance due to excessive template use, which causes structural collapse and hinders Na^+ transport and storage. In the Ragone plot [Figure 3F], NFP/C-HT$_{0.02}$ demonstrates higher energy and power densities than other recently reported NFP cathodes, highlighting its practical potential. Moreover, after 500 cycles at 1 A g^{-1} [Figure 3G], NFP/C-HT$_{0.02}$ retains a reversible capacity of 75.8 mAh g^{-1} with 77.8% capacity retention, confirming the advantages of its durable porous framework and optimized Na^+ insertion/extraction kinetics for long-term cycling.

Galvanostatic intermittent titration technique (GITT) measurements were performed to evaluate the Na^+ diffusion coefficients (D_{Na}+) of various samples [Supplementary Figure 13]. The NFP/C-HT$_{0.02}$ electrode exhibits a D_{Na}+ of 5.3 × 10^{-12} cm^2 s^{-1}, which is notably higher than that of bulk NFP (3.3 × 10^{-12} cm^2 s^{-1}). This enhancement can be attributed to the reduced particle size, which shortens the solid-state diffusion length, as well as the moderate lattice disorder induced by Jahn-Teller distortion, facilitating Na^+ migration within the crystal structure. To further assess the interfacial charge-transfer kinetics, temperature-dependent EIS was conducted from 293.15 to 313.15 K in 5 K intervals [Supplementary Figure 14A]. The Nyquist plots show a

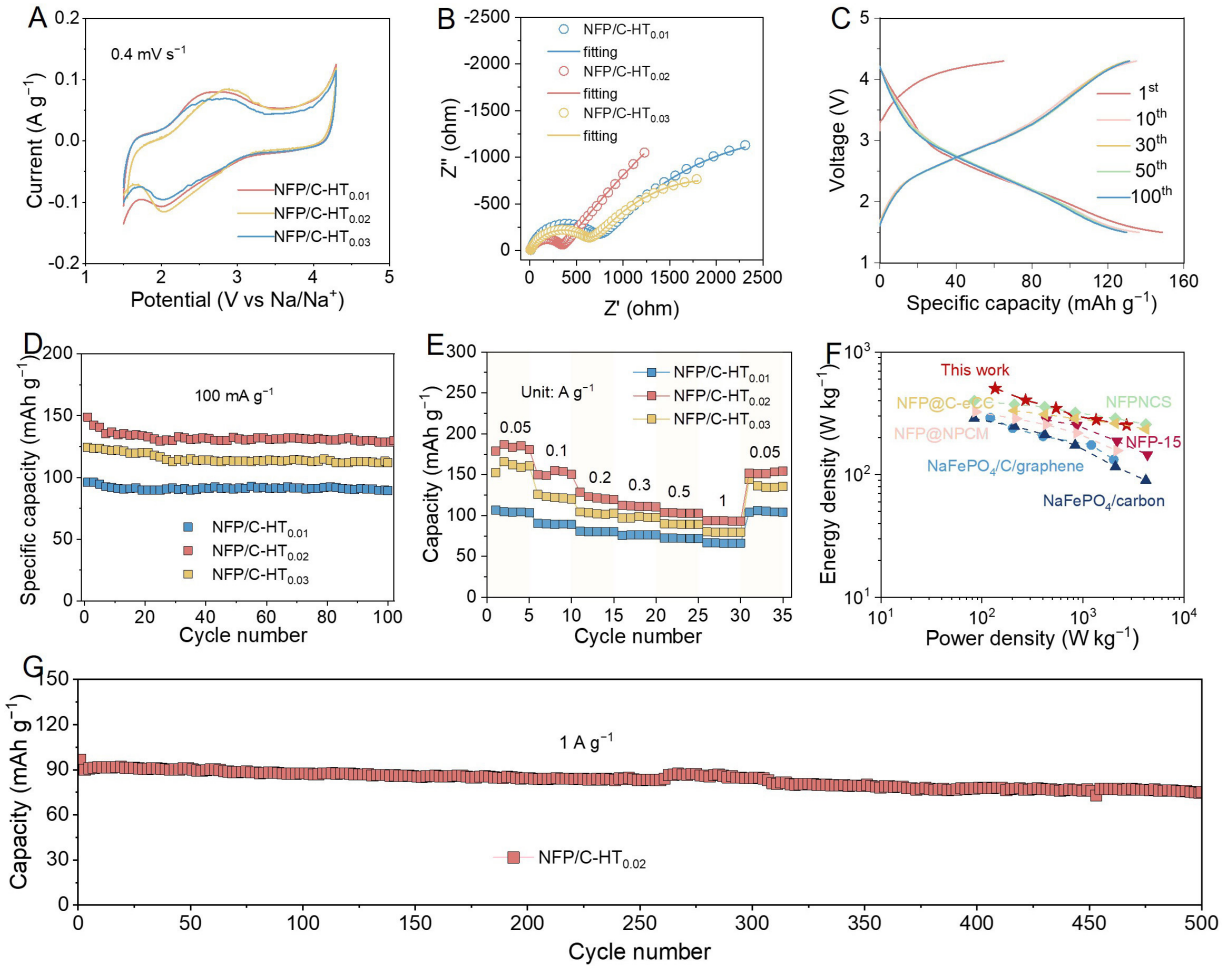

Figure 3. Electrochemical performance: (A and B) CV curves and EIS plots of NFP/C-HT$_{0.01}$, NFP/C-HT$_{0.02}$, and NFP/C-HT$_{0.03}$ samples; (C) charge and discharge curves of NFP/C-HT$_{0.02}$ at 100 mA g^{-1}; (D and E) cycling performance at a current density of 100 mA g^{-1} and rate performance of NFP/C-HT$_{0.01}$, NFP/C-HT$_{0.02}$, and NFP/C-HT$_{0.03}$ samples; (F) Ragone plots of NFP/C-HT$_{0.02}$ and other NFP materials for SIBs[16,20-22,42,43]; (G) long-term cycling performance at 1 A g^{-1} of NFP/C-HT$_{0.02}$.

high-frequency semicircle whose diameter decreases markedly upon heating, indicating that *Rct* is strongly temperature-dependent. Arrhenius fitting of R_{ct}^{-1} yields an apparent activation energy of 0.417 eV [Supplementary Figure 14B], which is significantly lower than values reported for iron-based polyanion cathodes in the literature[44,45]. This quantitative agreement between the low E_a and the high D_{Na}+ from GITT demonstrates that both interfacial charge transfer and bulk ionic diffusion are synergistically optimized in NFP/C-HT$_{0.02}$.

DISCUSSION

Relationship between structural evolution and electrochemical performance

Ex situ XRD and *in situ* EIS analyses of NFP/C-HT$_{0.02}$ were performed to elucidate the relationship between structural evolution and electrochemical performance. During the discharge process, the diffraction peaks at 33° and 35°, corresponding to the (121) and (301) crystal planes, respectively, showed no significant shift, indicating excellent structural stability of the sample. Notably, when discharged below 2.5 V, these two peaks gradually broadened, primarily due to the reduction of Fe^{3+} to Fe^{2+}. The strong Jahn-Teller distortion associated with Fe^{2+} causes the structure to deviate from ideal octahedral coordination, resulting in decreased crystallinity and increased amorphous characteristics of the material [Figure 4A]. The corresponding evolution of the unit cell volume is shown in Figure 4B, displaying an initial contraction followed by

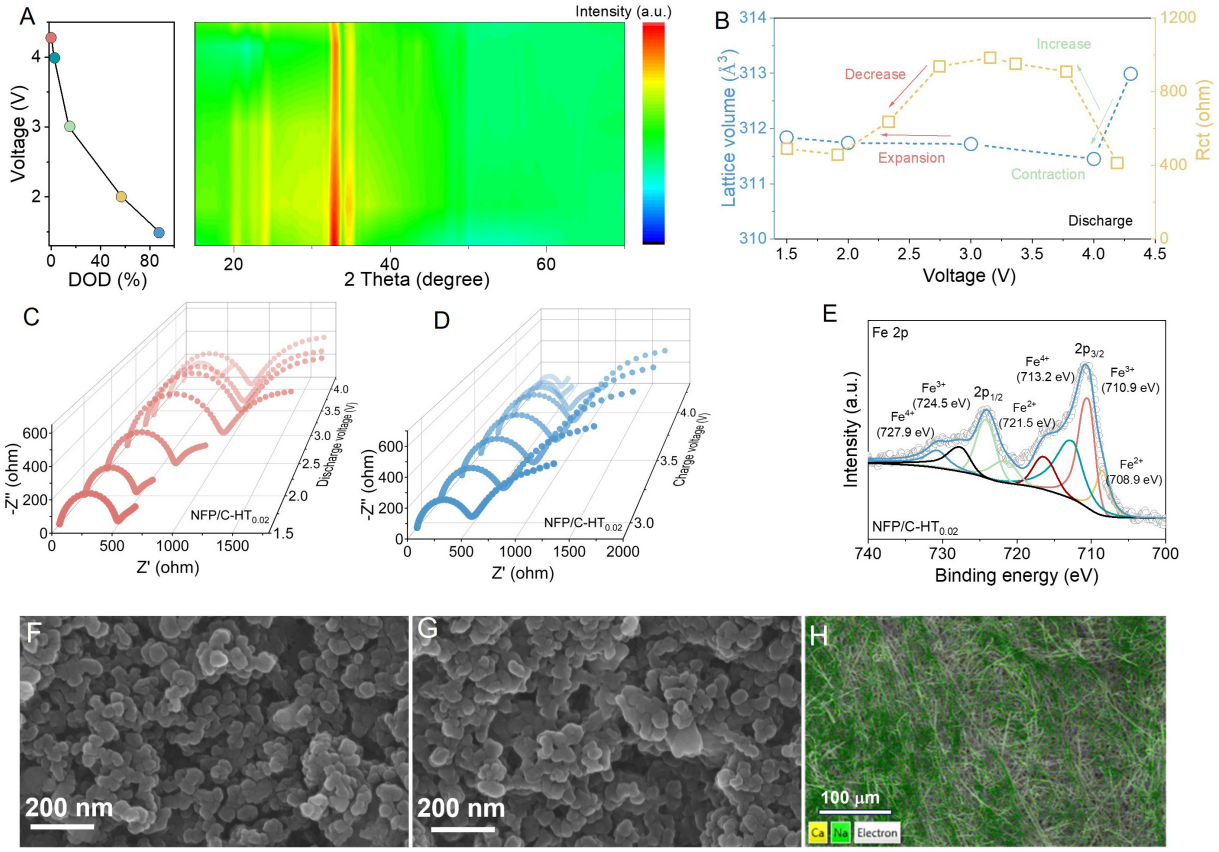

Figure 4. (A) Investigation of the sodium-storage mechanism: *Ex situ* XRD of NFP/C-HT$_{0.02}$ during discharge; (B) evolution of the unit cell volume and *in situ* impedance *Rct* of NFP/C-HT$_{0.02}$ during discharge; *in situ* EIS spectra of NFP/C-HT$_{0.02}$ during discharge (C) and charge (D); (E) Fe 2p spectra of NFP/C-HT$_{0.02}$ after charging; SEM images of NFP/C-HT$_{0.02}$ after charging (F) and after long-term cycling (G); (H) elemental mapping of the metallic sodium surface on the counter electrode after charging of NFP/C-HT$_{0.02}$.

expansion, which correlates with the *in situ* EIS results during the discharge process [Figure 4C]. The *in situ* EIS spectra of NFP/C-HT$_{0.02}$ during discharge [Figure 4C] reveal a clear decrease in *Rct* below 2.5 V. This decline is attributed to the stronger Jahn-Teller effect of Fe^{2+} compared to Fe^{3+}, which induces greater structural disorder and unit cell expansion, thereby accelerating the electrode's charge transfer rate.

It should be noted that in a well-ordered structure, whether composed entirely of symmetric units (e.g., $Fe^{3+}O_6$, PO_4) or entirely of asymmetric units (e.g., $Fe^{2+}O_6$), the stability of the structure is determined by these fundamental building blocks. If unstable factors arise, specifically a mixed phase containing both symmetric and asymmetric units (e.g., $Fe^{2+}O_6$, $Fe^{3+}O_6$, or even $Fe^{4+}O_6$), the overall structural stability is compromised. This results in dynamic Jahn-Teller disorder, which prevents the structure from maintaining a stable phase consistent with thermodynamic equilibrium. Instead, the system undergoes continuous transformations between dynamically unstable phases, resembling a metastable equilibrium state.

The *in situ* EIS results during the charging process are presented in Figure 4D. As the charging voltage increases, the *Rct* gradually rises, primarily due to the oxidation of Fe^{2+} to Fe^{3+} and the relatively weak Jahn-Teller effect associated with Fe^{3+}. When the voltage exceeds 4.0 V, *Rct* decreases significantly. This decrease can be attributed to the formation of Fe^{4+} ($t_{2g}^3e_g^1$), which exhibits an extremely strong Jahn-Teller effect, causing distortion and deformation of the sample structure and thereby creating more Na^+ transport channels. The fitted results of the *in situ* EIS spectra at various charging voltages are shown in Supplementary Figure 15. To verify the oxidation of Fe^{3+} to Fe^{4+} during charging, high-resolution Fe 2p XPS

spectra were collected after the process. The presence of distinct Fe^{4+} peaks in Figure 4E provides direct evidence of this reaction. The valence change of iron induces a structural transition toward an amorphous state, which enhances Na^+ migration and interface reactivity, thereby significantly improving the electrochemical kinetics of the electrode material[46,47].

The dynamic Jahn-Teller effect maintains the material in a distorted state, facilitating rapid Na^+ migration. Schematic structures with different iron valences are shown in Supplementary Figure 16. Although dynamic Jahn-Teller lattice distortion occurs continuously during cycling, NFP/C-$HT_{0.02}$ retains a uniform and intact nanospherical morphology without particle cracking or pulverization after charging and extended cycling [Figure 4F and G]. This remarkable structural stability results from the high surface charge density of the particles, which inhibits the agglomeration of ultrafine nanoparticles through electrostatic repulsion. The hierarchical pores accommodate lattice volume variations caused by Na^+ deintercalation and intercalation, while the continuous outer carbon coating preserves the integrity of the conductive network. The synergy of these three factors mitigates internal stress accumulation during cycling.

Elemental mapping of the metallic sodium surface on the counter electrode after charging NFP/C-$HT_{0.02}$ is shown in Figure 4H. Notably, calcium was detected alongside sodium. Since physical adsorption on the anode has been accounted for, the calcium signal must originate from the extraction of Ca^{2+} ions from the cathode during charging. This finding corresponds with the observed higher initial charging capacity, which exceeds the theoretical value, confirming the successful Ca^{2+} doping of the NFP/C-$HT_{0.02}$ lattice. Although the standard electrode potential of Ca^{2+}/Ca (-2.87 V *vs.* SHE) is more negative than that of Na^+/Na (-2.71 V *vs.* SHE), kinetic factors, including interfacial polarization and local potential changes during Na^+ extraction, enable partial co-migration of Ca^{2+} during charging. The resulting calcium deposition (1.55 on the Mohs hardness scale) on the sodium metal surface (0.4 on the Mohs hardness scale) can also suppress dendrite growth. Furthermore, the stable incorporation of larger Ca^{2+} ions expands Na^+ migration pathways within the lattice structure, enhancing the ionic transport kinetics of maricite NFP[48,49].

Multiscale activation of electrochemically inert materials

Throughout the entire text, a multiscale and universal strategy to activate these potentially electrochemically inert materials is proposed as follows.

(1) Configuring intrinsic structural disorder. The dynamic Jahn-Teller effect in transition metal ions (e.g., Fe^{2+}, Mn^{3+}) induces persistent lattice distortions during cycling[50,51]. This disrupts long-range order and promotes an amorphous-like structure, creating widened three-dimensional ion migration channels that lower diffusion barriers and enhance intrinsic electrochemical activity[52,53]. Other chemical methods can also increase the intrinsic disorder of crystal structures. For example, high-entropy design, where multiple principal elements cause significant lattice distortion, leading to chemical structural disorder; doping, which introduces vacancies and point defects that cause lattice relaxation; and non-equilibrium preparation, which limits atomic migration to form metastable disorder.

(2) Reconstructing external material disorder (i.e., altering particle size and morphology). Manual nanosizing of the material not only creates more active sites but also introduces cation and oxygen vacancies. These defects generate preferential migration pathways and additional active centers, while synergistically shortening ion and electron transport distances to enhance external disorder[54,55]. This paper introduces nanostructures through chemical methods such as templating agents and acid etching. In practical production, a series of high-entropy oxides or ceramics can be prepared using methods like co-precipitation, sol-gel, and mechanochemical synthesis. Additionally, alloy-type materials can be obtained through techniques such as arc melting, mechanical alloying, and magnetron sputtering. Rapid quenching or melt

spinning is also a classic and commonly used method for preparing amorphous alloys (metallic glasses). Through the mechanical impact and shear forces provided by high-energy ball milling, powder particles of different materials continuously undergo plastic deformation, cold welding, and fracture, eventually diffusing and mixing at the atomic scale. This is our most fundamental method for inducing external structural disorder.

(3) Achieving interface and process stabilization. First, interactions between particles must be minimized to enhance overall flowability. For example, a high surface charge (zeta potential) prevents particle aggregation through electrostatic repulsion. Dispersants firmly adsorb onto particle surfaces via "anchor groups," while their long chains extend into the solvent, forming a protective layer. The physical overlap of these long chains and the resulting entropic repulsion generate a strong repulsive force. Surface coatings (e.g., carbon, polymers), elemental doping, and heterostructure construction create conductive networks that improve electron transfer and cycling stability[56,57]. Through process optimization, such as refining powder characteristics, ensuring thorough mechanical dispersion, using an appropriate feeding sequence, and judiciously applying other additives, strong repulsive forces can be introduced between particles, surpassing van der Waals attractions. This enables particles to remain stable and uniformly dispersed in the solvent, effectively achieving "de-agglomeration." Such slurries exhibit low viscosity, good flowability, and desirable rheological properties, including shear thinning.

In summary, the coordinated implementation of internal structural disorder and external material disorder, combined with interface stabilization, constitutes an effective "internal-external" synergistic strategy. This multiscale approach systematically optimizes charge and ion transport pathways, providing a general principle for developing high-performance electrochemical energy materials.

CONCLUSIONS

In summary, this work successfully activates the typically inert maricite NFP through a synergistic multiscale design. The introduction of Ca^{2+} doping broadens the Na^{+} transport channels, while the dynamic Jahn-Teller effect, arising from mixed-valence Fe ions, induces beneficial internal lattice distortions. Coupled with external disorder introduced *via* nanocrystallization, which shortens ion diffusion paths, the resulting $Na_{0.33}Fe_{0.95}Ca_{0.06}PO_4$ cathode exhibits remarkable electrochemical performance, achieving a high reversible capacity of 178.6 mAh g^{-1} and an impressive material-based energy density of 415 Wh kg^{-1}. This study not only demonstrates a feasible pathway to unlock the potential of maricite-type cathodes but also provides a general strategy for activating electrochemically inert materials, paving the way for the development of sustainable and high-performance sodium-ion batteries.

DECLARATIONS

Authors' contributions

Designed and conducted the experiments, interpreted the results, and wrote the manuscript: Hu, W.; Dong, S.

Assisted with data interpretation and reviewed and edited the manuscript: Zhang, Y.; Tang, B.

Contributed to data collection and analysis: Wu, Y.; Li, J.

Provided methodology and supervision: Zhou, Z.

Supported the experimental setup and offered guidance throughout the research process: Tang, Y.; Liu, L.

Availability of data and materials

The data supporting the findings of this study are available within this Article and its Supplementary Materials. Further data are available from the corresponding authors upon request.

AI and AI-assisted tools statement

During the preparation of this manuscript, the AI tool DeepSeek-V3 (version V3, released 2024-12-26) was used solely for language editing. The tool did not influence the study design, data collection, analysis,

interpretation, or the scientific content of the work. All authors take full responsibility for the accuracy, integrity, and final content of the manuscript.

Financial support and sponsorship

Hu, W.; Dong, S. contributed equally to this work. This work was supported by the National Natural Science Foundation of China (22368047, 22468048, 22508330), the Funded by the Xinjiang Talent Development Fund (XJRC-2025-KJ-PY-KJLJ-016), the "Tianshan Talents" Science and Technology Innovation Team of Xinjiang Uygur Autonomous Region (2024TSYCTD0002), and the Natural Science Foundation of Henan Province (252300423746).

Conflicts of interest

All authors declared that there are no conflicts of interest.

Ethical approval and consent to participate

Not applicable.

Consent for publication

Not applicable.

Copyright

© The Author(s) 2026.

Supplementary Materials

Supplementary Materials

REFERENCES

1. Sada, K.; Darga, J.; Manthiram, A. Challenges and prospects of sodium-ion and potassium-ion batteries for mass production. *Adv. Energy. Mater.* **2023**, *13*, 2302321. DOI
2. Zhao, Y.; Kang, Y.; Wozny, J.; et al. Recycling of sodium-ion batteries. *Nat. Rev. Mater.* **2023**, *8*, 623-34. DOI
3. Usiskin, R.; Lu, Y.; Popovic, J.; et al. Fundamentals, status and promise of sodium-based batteries. *Nat. Rev. Mater.* **2021**, *6*, 1020-35. DOI
4. Singh, A. N.; Islam, M.; Meena, A.; et al. Unleashing the potential of sodium-ion batteries: current state and future directions for sustainable energy storage. *Adv. Funct. Mater.* **2023**, *33*, 2304617. DOI
5. Li, S.; Zhao, Y.; Dang, Q.; Qin, J.; Hu, Q. Research progress on LT performance of sodium-ion battery electrolytes. *Energy. Mater.* **2026**, *6*, 600021. DOI
6. Liao, H.; Zhang, Z.; Zheng, Y.; Gao, Y. $NaFePO_4$ for sodium-ion batteries: mechanism, synthesis and optimization strategies toward commercialization. *Energy. Storage. Mater.* **2024**, *65*, 103157. DOI
7. Zhang, Z.; Du, Y.; Wang, Q. C.; et al. A yolk-shell-structured $FePO_4$ cathode for high-rate and long-cycling sodium-ion batteries. *Angew. Chem. Int. Ed.* **2020**, *59*, 17504-10. DOI
8. Kim, J.; Seo, D.; Kim, H.; et al. Unexpected discovery of low-cost maricite $NaFePO_4$ as a high-performance electrode for Na-ion batteries. *Energy. Environ. Sci.* **2015**, *8*, 540-5. DOI
9. Guo, Z.; Yao, X.; Tian, H.; Cai, Y.; Su, Z. Effect of Zn-doping on the electrochemical performance of NaFePO4/C cathode material for lithium ion battery. *Int. J. Electrochem. Sci.* **2021**, *16*, 210758. DOI
10. Tang, W.; Song, X.; Du, Y.; et al. High-performance $NaFePO_4$ formed by aqueous ion-exchange and its mechanism for advanced sodium ion batteries. *J. Mater. Chem. A.* **2016**, *4*, 4882-92. DOI
11. Hwang, J.; Matsumoto, K.; Orikasa, Y.; et al. Crystalline maricite $NaFePO_4$ as a positive electrode material for sodium secondary batteries operating at intermediate temperature. *J. Power. Sources.* **2018**, *377*, 80-6. DOI
12. Avdeev, M.; Mohamed, Z.; Ling, C. D.; et al. Magnetic structures of $NaFePO_4$ maricite and triphylite polymorphs for sodium-ion batteries. *Inorg. Chem.* **2013**, *52*, 8685-93. DOI
13. Zaghib, K.; Trottier, J.; Hovington, P.; et al. Characterization of Na-based phosphate as electrode materials for electrochemical cells. *J. Power. Sources.* **2011**, *196*, 9612-7. DOI
14. Kapaev, R.; Chekannikov, A.; Novikova, S.; et al. Mechanochemical treatment of maricite-type $NaFePO_4$ for achieving high electrochemical performance. *J. Solid. State. Electrochem.* **2017**, *21*, 2373-80. DOI

15. Hilder, M.; Howlett, P. C.; Saurel, D.; et al. Stable cycling of $NaFePO_4$ cathodes in high salt concentration ionic liquid electrolytes. *J. Power. Sources.* **2018**, *406*, 70-80. DOI
16. Ma, X.; Xia, J.; Wu, X.; Pan, Z.; Shen, P. K. Remarkable enhancement in the electrochemical activity of maricite $NaFePO_4$ on high-surface-area carbon cloth for sodium-ion batteries. *Carbon* **2019**, *146*, 78-87. DOI
17. Zhu, Y.; Xu, Y.; Liu, Y.; Luo, C.; Wang, C. Comparison of electrochemical performances of olivine $NaFePO_4$ in sodium-ion batteries and olivine $LiFePO_4$ in lithium-ion batteries. *Nanoscale* **2013**, *5*, 780-7. DOI
18. Liu, Y.; Zhang, N.; Wang, F.; Liu, X.; Jiao, L.; Fan, L. Z. Approaching the downsizing limit of maricite $NaFePO_4$ toward high-performance cathode for sodium-ion batteries. *Adv. Funct. Mater.* **2018**, *28*, 1801917. DOI
19. Heubner, C.; Heiden, S.; Schneider, M.; Michaelis, A. In-situ preparation and electrochemical characterization of submicron sized $NaFePO_4$ cathode material for sodium-ion batteries. *Electrochim. Acta.* **2017**, *233*, 78-84. DOI
20. Liu, B.; Zhang, Q.; Li, L.; et al. Achieving highly electrochemically active maricite $NaFePO_4$ with ultrafine $NaFePO_4$@C subunits for high rate and low temperature sodium-ion batteries. *Chem. Eng. J.* **2021**, *405*, 126689. DOI
21. Rahman, M. M.; Sultana, I.; Mateti, S.; Liu, J.; Sharma, N.; Chen, Y. Maricite $NaFePO_4$/C/graphene: a novel hybrid cathode for sodium-ion batteries. *J. Mater. Chem. A.* **2017**, *5*, 16616-21. DOI
22. Wang, D.; Wu, Y.; Lv, J.; Wang, R.; Xu, S. Carbon encapsulated maricite $NaFePO_4$ nanoparticles as cathode material for sodium-ion batteries. *Colloids. Surf. A. Physicochem. Eng. Asp.* **2019**, *583*, 123957. DOI
23. Zhao, L.; Yu, L.; Wan, G.; et al. Co-manipulation of ultrafine nanostructure and uniform carbon layer activates maricite-structured $NaFePO_4$ as a high-performance cathode for sodium-ion batteries. *Small. Sci.* **2023**, *3*, 2300122. DOI PubMed PMC
24. Zhou, J.; Xing, C.; Huang, J.; et al. Direct upcycling of leached $FePO_4$ from spent lithium-ion batteries toward gradient-doped $LiMn_xFe_{1-x}PO_4$ cathode material. *Adv. Energy. Mater.* **2023**, *14*, 2302761. DOI
25. Meng, J.; Liu, X.; Li, J.; et al. General oriented synthesis of precise carbon-confined nanostructures by low-pressure vapor superassembly and controlled pyrolysis. *Nano. Lett.* **2017**, *17*, 7773-81. DOI
26. Gao, S.; He, Y.; Yue, G.; et al. Pea-like MoS_2@$NiS_{1.03}$-carbon heterostructured hollow nanofibers for high-performance sodium storage. *Carbon. Energy.* **2023**, *5*, e319. DOI
27. Song, X.; Li, S.; Sun, Q.; Yang, C.; Zhu, J. One-pot room-temperature synthesis of high-rate sodium vanadium oxyfluorophosphate positive electrode with high ionic and electronic conductivity for sodium-ion batteries. *Chem. Eng. J.* **2025**, *510*, 161617. DOI
28. Liang, Z.; Nafis, M. S.; Rodriguez, D.; Ban, C. Surface science and engineering for electrochemical materials. *Acc. Chem. Res.* **2024**, *57*, 3102-12. DOI PubMed
29. Zhao, W.; Dong, H.; Xing, Z.; et al. Advances and challenges of porous structure on solid-liquid interfaces in polyanionic sodium-ion batteries. *Adv. Energy. Mater.* **2024**, *14*, 2402720. DOI
30. Xu, L.; Liu, Y.; Hu, X.; Wu, Y.; Wen, Z.; Li, J. 3D hierarchical micro/nanostructures for sodium-based battery anode materials. *Acc. Mater. Res.* **2024**, *5*, 822-35. DOI
31. Yang, Z.; Katsuyama, Y.; Huang, A.; et al. Ultrafast sodium-ion batteries based on vanadium oxide and laser-scribed graphene electrodes. *Chem. Mater.* **2024**, *36*, 8359-68. DOI
32. Han, L.; Chen, K.; Chen, X.; et al. A 3.7 V amorphous $Na_2VO(SO_4)_2$ cathode with boosted electrode kinetics for advanced sodium-ion batteries. *Nano. Energy.* **2025**, *139*, 110986. DOI
33. Zhang, X.; Yin, X.; Xie, J.; et al. Lanthanum-doped $Na_4Fe_3(PO_4)_2P_2O_7$/C as cathode materials in sodium-ion batteries: enhanced ion diffusion kinetics and embedded pseudocapacitance. *J. Power. Sources.* **2025**, *635*, 236531. DOI
34. Ma, R.; Meng, J.; Su, X.; et al. A bifunctional Na-deficient strategy induced pure phase $Na_xFe_3(PO_4)_2P_2O_7$ cathode with high capacity for sodium-ion batteries. *J. Mater. Chem. A.* **2025**, *13*, 2631-41. DOI
35. Zhao, X.; Geng, S.; Zhou, T.; et al. Unlocking deep and fast potassium-ion storage through phosphorus heterostructure. *Small* **2023**, *19*, 2301750. DOI
36. Liang, Y.; Xu, L.; Chen, Z.; Ning, D.; Sun, Z. Recent research progress in the application of $Na_3V_2(PO_4)_2F_3$ cathode materials in sodium-ion batteries: synthesis, modification, and battery optimization. *Energy. Mater.* **2025**, *5*, 500115. DOI
37. Li, Z.; Deng, L.; Kinloch, I. A.; Young, R. J. Raman spectroscopy of carbon materials and their composites: graphene, nanotubes and fibres. *Prog. Mater. Sci.* **2023**, *135*, 101089. DOI
38. Li, H.; Wang, X.; Liu, F.; et al. Reduced bond covalency and anisotropic lattice distortion enable high Fe-Mn redox activation in a mixed-polyanionic cathode. *ACS. Nano.* **2025**, *19*, 35712-23. DOI
39. Fei, W.; Zhang, X.; Sun, K.; et al. Dual-site defects engineering to eliminate impurities and optimize reversible reaction kinetics of $Na_4Fe_3(PO_4)_2P_2O_7$ cathode for superior performance sodium ion batteries. *Energy. Storage. Mater.* **2024**, *73*, 103848. DOI

40. Halldin, Stenlid. J.; Görlin, M.; Diaz-Morales, O.; et al. Operando characterization of Fe in doped $Ni_x(Fe_x)O_yH_z$ catalysts for electrochemical oxygen evolution. *J. Am. Chem. Soc.* **2025**, *147*, 4120-34. DOI
41. Wang, Z.; Song, Y.; Wang, J.; et al. Vanadium oxides with amorphous-crystalline heterointerface network for aqueous zinc-ion batteries. *Angew. Chem. Int. Ed.* **2023**, *62*, e202216290. DOI
42. Liu-Théato, X.; Indris, S.; Hua, W.; et al. Self-standing, collector-free maricite $NaFePO_4$/carbon nanofiber cathode endowed with increasing electrochemical activity. *Energy. Fuels.* **2021**, *35*, 18768-77. DOI
43. Xiong, F.; An, Q.; Xia, L.; et al. Revealing the atomistic origin of the disorder-enhanced Na-storage performance in $NaFePO_4$ battery cathode. *Nano. Energy.* **2019**, *57*, 608-15. DOI
44. Heubner, C.; Heiden, S.; Matthey, B.; Schneider, M.; Michaelis, A. Sodiation vs. lithiation of $FePO_4$: a comparative kinetic study. *Electrochim. Acta.* **2016**, *216*, 412-9. DOI
45. Kavaliukė, V.; Nesterova, I.; Kežionis, A.; et al. Combined conductivity and electrochemical impedance spectroscopy study of $Na_2FeP_2O_7$ cathode material for sodium ion batteries. *Solid. State. Ion.* **2022**, *385*, 116024. DOI
46. Li, Y. J.; Zhu, Y. F.; Chen, B. B.; et al. Jahn-teller effect in sodium layered oxide cathodes: inducement mechanisms, mitigation strategies, and rational utilizations. *Adv. Funct. Mater.* **2025**, *35*, 2504096. DOI
47. Sun, J.; Meng, X.; Hui, Y.; et al. Structurally controlled $Na_4VMn(PO_4)_3$ cathodes via alkali metal cation substitution for high-performance sodium-ion batteries. *Nano. Energy.* **2025**, *134*, 110587. DOI
48. Hogrefe, K.; Königsreiter, J.; Bernroitner, A.; Gadermaier, B.; Ashbrook, S. E.; Wilkening, H. M. R. Length-scale-dependent ion dynamics in Ca-doped Na_3PS_4. *Chem. Mater.* **2024**, *36*, 980-93. DOI
49. Glück, H.; Morscher, A.; Hallweger, S. A.; Kieslich, G.; Zeier, W. G. On the high-temperature Ca^{2+} conduction in NASICON-type $Ca_xIn_xZr_x(PO_4)_3$. *Chem. Mater.* **2025**, *37*, 8392-402. DOI
50. Ashraf, M. A.; Javid, A.; Kim, J.; Park, C. Structurally stable P3-type $K_{0.45}MnO_2$ cathode with a $KTaO_3$ protective layer for high-performance potassium-ion batteries. *Energy. Storage. Mater.* **2025**, *80*, 104387. DOI
51. Li, F.; Gu, X.; Cui, A.; et al. In situ structure modulation of cathode-electrolyte interphase for high-performance potassium-ion battery. *Adv. Funct. Mater.* **2024**, *34*, 2313146. DOI
52. Li, Z.; Ning, F.; Ma, X.; et al. Manganese vacancy motivated structural disorder-to-order transformation to boost fast-charging and long-lasting sodium-ion battery P2-type layered cathode. *Energy. Storage. Mater.* **2025**, *76*, 104114. DOI
53. Li, X.; Yu, S.; Zhao, X.; Liu, J. Structural stability of layered oxides for sodium-ion batteries: insights and strategies. *Energy. Storage. Mater.* **2025**, *79*, 104303. DOI
54. Liu, Y.; Zhang, C.; Lin, L.; et al. Intrinsic highly conductive and mechanically robust Li-rich cathode materials enabled by microstructure engineering for enhanced electrochemical properties. *Adv. Funct. Mater.* **2023**, *34*, 2308494. DOI
55. Li, S.; Liu, Y.; Zhang, Y.; et al. Multi-functionalized full-interface integrated engineering towards highly reversible Li-rich Mn-based cathode. *Energy. Storage. Mater.* **2024**, *66*, 103241. DOI
56. Muruganantham, R.; Tseng, T.; Lee, M.; Kheawhom, S.; Liu, W. Artificial interface modification of Ni-rich ternary cathode material to enhance electrochemical performance for Li-ion storage through RF-plasma-assisted technique. *Chem. Eng. J.* **2023**, *464*, 142686. DOI
57. Liang, Y.; Liu, W.; Tang, Z.; Qin, M.; Wu, H.; Zeng, J. Enhancing electrochemical properties of O3-type $NaNi_{1/3}Fe_{1/3}Mn_{1/3}O_2$ cathode material for sodium-ion batteries via regulation of precursor's growth environment. *Chem. Eng. J.* **2025**, *516*, 164118. DOI

Disclaimer/Publisher's Note: All statements, opinions, and data contained in this publication are solely those of the individual author(s) and contributor(s) and do not necessarily reflect those of OAE and/or the editor(s). OAE and/or the editor(s) disclaim any responsibility for harm to persons or property resulting from the use of any ideas, methods, instructions, or products mentioned in the content.

© The Author(s) 2026. Open Access This article is licensed under a Creative Commons Attribution 4.0 International License (https://creativecommons.org/licenses/by/4.0/), which permits unrestricted use, sharing, adaptation, distribution and reproduction in any medium or format, for any purpose, even commercially, as long as you give appropriate credit to the original author(s) and the source, provide a link to the Creative Commons license, and indicate if changes were made.